

# 1 Super-resolution fight club: Assessment of 2D & 3D single- 2 molecule localization microscopy software

3 *Daniel Sage*<sup>\*+1</sup>, *Thanh-An Pham*<sup>+1</sup>, *Hazen Babcock*<sup>2</sup>, *Tomas Lukes*<sup>3,4</sup>, *Thomas Pengo*<sup>5</sup>, *Jerry Chao*<sup>6,7</sup>, *Ramraj*  
4 *Velmuruga*<sup>7,8</sup>, *Alex Herbert*<sup>9</sup>, *Anurag Agrawal*<sup>10</sup>, *Silvia Colabrese*<sup>1,11</sup>, *Ann Wheeler*<sup>12</sup>, *Anna Archetti*<sup>13</sup>, *Bernd*  
5 *Rieger*<sup>14</sup>, *Raimund Ober*<sup>6,7,15</sup>, *Guy M. Hagen*<sup>16</sup>, *Jean-Baptiste Sibarita*<sup>17,18</sup>, *Jonas Ries*<sup>19</sup>, *Ricardo Henriques*<sup>20</sup>,  
6 *Michael Unser*<sup>1</sup>, *Seamus Holden*<sup>\*+21</sup>

7 \*Corresponding authors: [daniel.sage@epfl.ch](mailto:daniel.sage@epfl.ch), [seamus.holden@ncl.ac.uk](mailto:seamus.holden@ncl.ac.uk).

8 +Equal contribution

- 9 1: Biomedical Imaging Group, School of Engineering, Ecole Polytechnique Fédérale de Lausanne  
10 (EPFL), Switzerland  
11 2: Harvard Center for Advanced Imaging, Harvard University, Cambridge, Massachusetts, USA  
12 3: Laboratory of Nanoscale Biology & Laboratoire d'Optique Biomédicale, STI - IBI, EPFL, Lausanne,  
13 Switzerland  
14 4: Department of Radioelectronics, FEE, Czech Technical University, Prague, Czech Republic  
15 5: University of Minnesota Informatics Institute, University of Minnesota Twin Cities, USA  
16 6: Department of Biomedical Engineering, Texas A&M University, College Station, Texas, USA  
17 7: Department of Molecular and Cellular Medicine, Texas A&M University Health Science Center,  
18 College Station, Texas, USA  
19 8: Department of Microbial Pathogenesis and Immunology, Texas A&M University Health Science  
20 Center, Bryan, Texas, USA  
21 9: MRC Genome Damage and Stability Centre, School of Life Sciences, University of Sussex, Brighton,  
22 UK  
23 10 : Double Helix LLC, Boulder, Colorado, USA  
24 11 : Istituto Italiano di Tecnologia, Genova, Italy  
25 12: Advanced Imaging Resource, Institute of Genetics and Molecular Medicine, University of  
26 Edinburgh, Edinburgh, UK  
27 13 : Laboratory of Experimental Biophysics, École Polytechnique Fédérale de Lausanne (EPFL),  
28 Lausanne, Switzerland  
29 14: Department of Imaging Physics, Delft University of Technology, The Netherlands  
30 15: Centre for Cancer Immunology, University of Southampton, Southampton, UK  
31 16: UCCS center for the Biofrontiers Institute, University of Colorado at Colorado Springs, Colorado,  
32 USA  
33 17: Interdisciplinary Institute for Neuroscience, University of Bordeaux, Bordeaux, France  
34 18: Interdisciplinary Institute for Neuroscience, Centre National de la Recherche Scientifique (CNRS)  
35 UMR 5297, Bordeaux, France  
36 19: European Molecular Biology Laboratory (EMBL), Cell Biology and Biophysics Unit, Heidelberg,  
37 Germany  
38 20: Quantitative Imaging and Nanobiophysics Group, MRC Laboratory for Molecular Cell Biology,  
39 University College London, UK  
40 21: Centre for Bacterial Cell Biology, Institute for Cell and Molecular Biosciences, Newcastle  
41 University, UK

42 **ABSTRACT**

43 With the widespread uptake of 2D and 3D single molecule localization microscopy, a large set of  
44 different data analysis packages have been developed to generate super-resolution images. To guide  
45 researchers on the optimal analytical software for their experiments, in a large community effort we  
46 designed a competition to extensively characterise and rank these options. We generated realistic  
47 simulated datasets for popular imaging modalities – 2D, astigmatic 3D, biplane 3D, and double helix  
48 3D – and evaluated 36 participant packages against these data. This provides the first broad  
49 assessment of 3D single molecule localization microscopy software, provides a holistic view of how  
50 the latest 2D and 3D single molecule localization software perform in realistic conditions, and  
51 ultimately provides insight into the current limits of the field.

## 52 INTRODUCTION

53 Image processing software is central to single molecule localization microscopy (SMLM<sup>1-3</sup>). Efficient  
54 and automated image processing is essential to extract the super-resolved positions of individual  
55 molecules from thousands of raw microscope images, containing millions of blinking fluorescent  
56 spots. Improvements in SMLM image processing have been crucial in maximizing spatial resolution  
57 and reducing imaging time of SMLM for compatibly with live cell imaging<sup>4-6</sup>. If SMLM is to achieve a  
58 resolving power approaching that of electron microscopy, the analysis software employed needs to  
59 be robust, accurate, and performing at current algorithmic limits. This can only be achieved through  
60 rigorous quantification of SMLM software performance.

61 The first localization microscopy software challenge was carried out in 2013 to benchmark 2D SMLM  
62 software<sup>7</sup>. But biology is not just a 2D problem, and a key focus of localization microscopy is the  
63 imaging of 3D imaging of nanoscale cellular processes<sup>8,9</sup>. 3D localization microscopy is a more  
64 difficult image processing problem than 2D SMLM. In addition to finding the center of diffraction  
65 limited spots to super-resolve lateral position, 3D SMLM algorithms must also extract axial  
66 information from the image, usually by measuring small changes in the shape of a point spread  
67 function<sup>10</sup> (PSF).

68 Despite the widespread use of 3D localization microscopy, and challenging nature of 3D SMLM  
69 image processing, the performance of software for 3D single molecule localization microscopy has  
70 previously only been assessed for 2-3 software packages at a time, and without standard test data or  
71 metrics<sup>11-14</sup>. In the absence of common reference datasets and reliable assessment, it is not possible  
72 to objectively assess how different software affects final image quality, or which algorithmic  
73 approaches are most successful. Crucially, end-users cannot determine which 3D SMLM software  
74 package and imaging modality is optimal for their application.

75 We therefore ran the first 3D localization microscopy software challenge, to assess the performance  
76 of 3D SMLM software. We assessed software performance on simulated datasets designed for  
77 maximum realism, incorporating experimentally derived point spread functions, using biologically  
78 inspired structures, signal to noise levels based closely on common experimental conditions, and  
79 modelling fluorophore photophysics. We assessed software performance on synthetic datasets for  
80 three popular 3D SMLM modalities: astigmatic imaging<sup>10</sup>, biplane imaging<sup>15</sup> and double helix point  
81 spread function microscopy<sup>16</sup>. We also assessed astigmatism software performance on two real  
82 STORM datasets. Furthermore, we ran a second 2D localization microscopy software challenge to  
83 assess performance of the latest 2D SMLM software.

## 84 RESULTS

### 85 Competition design

86 We established a broad committee from the SMLM community, including experimentalists and  
87 software developers, to define the scope of the challenge, ensure realism of the datasets and define  
88 analysis metrics. We opened this discussion to all interested parties in an online discussion forum<sup>17</sup>.

89 In 2016, we ran a first round of the 3D SMLM competition with explicit submission deadlines,  
90 culminating in a special session at the 6th annual Single Molecule Localization Microscopy  
91 Symposium (SMLMS 2016). Since then, the challenge has been opened to continuously accept new  
92 entries. Thirty-six software packages have been entered in the competition thus far, including four  
93 packages used in commercial software (**Table S1, Supplementary Note 1**). Participation in the  
94 competition actually led at least eight teams to modify their software to support additional 3D  
95 SMLM modalities, showing how competition can foster microscopy software development.

### 96 Realistic 3D simulations

97 Testing super-resolution software on experimental data lacks the ground truth information required  
98 for rigorous quantification of software performance. Therefore, realistic simulated datasets are

99 required. A critical challenge to in simulating 3D SMLM data was to accurately model the  
100 experimental microscope PSF for each 3D modality. 3D SMLM inherently involves addition of  
101 aberrations to the microscope PSF to encode the Z-position of the molecule. For the PSF models  
102 included in the competition: astigmatic (AS), double helix (DH), and biplane (BP), we observed that  
103 the PSFs showed complex aberrations not well described by simple analytical models (**Fig. S1**). Even  
104 experimental 2D PSFs showed significant aberrations away from the focal plane (**Fig. S1**).

105 We thus combined experimental 3D PSFs with simulated ground truth by performing simulations  
106 using PSFs directly derived from experimental calibration data (**Fig. 1, Methods**). We generated  
107 simulated datasets over a range of spot densities and signal to noise levels, for simulated  
108 microtubule- and endoplasmic reticulum-like structures, using a 4-state model for photophysics<sup>18</sup>  
109 (**Methods**).

## 110 **Quantitative performance assessment of 3D software**

111 We assessed software performance by 26 quality metrics (**Supplementary Note 2**). The complete set  
112 of summary statistics, axially resolved performance and super-resolved images is available for each  
113 competition software on the competition website. We built an interactive ranking and graphing  
114 interface for ranking and plotting software performance by any metric, including new user defined  
115 metrics (**Fig. S2**). Detailed individual software reports can also be accessed, along with a tool for  
116 side-by-side comparison of software (**Fig. S2, S3**).

117 We focused our primary analysis on metrics directly assessing performance in detecting individual  
118 molecules. This was based on three key metrics (**Methods**):

- 119 1. *Root mean squared localization error* (RMSE) between measured molecule position and the  
120 ground truth.
- 121 2. *Jaccard index* (JAC). This quantifies the fraction of correctly detected molecules in a dataset.
- 122 3. *Efficiency* (*E*). For ranking purposes, we developed a single summary statistic for overall  
123 evaluation of software performance combining RMSE and Jaccard index, which we term the  
124 *efficiency* (**Methods**).

125 Choice of ranking metric is discussed in **Supplementary Note 2**, where several alternative ranking  
126 metrics are also presented.

## 127 **Performance of 3D software**

128 Complete rankings for each imaging modality and spot density are presented (**Fig. 2**), together with  
129 summary information on all competition software (**Supplementary Table 1, Supplementary Note 1**).

130 After assembling an overall summary of best performers for each competition category, we  
131 investigated the performance of software within each imaging modality.

### 132 *Astigmatic localization microscopy*

133 Astigmatic localization microscopy is probably the most popular 3D SMLM modality, reflected by the  
134 highest number of software submissions in the 3D competition (**Fig. 2**). For astigmatism, we  
135 observed a large spread of software performance, even for the most straightforward high SNR, low  
136 spot density (LD) conditions (**Fig. 3, Supplementary Table 2**). The best-in-class software (SMAP-  
137 2018<sup>19</sup>) has significantly better localization error and Jaccard index performance than average  
138 (lateral RMSE 26 nm best vs 38 nm average, axial RMSE 29 nm best vs 66 nm average, Jaccard index  
139 85 % best vs 74 % average). Clearly, the quality of the image reconstruction depends strongly on  
140 choice of 3D software.

141 To investigate the reasons for software variation, we inspected plots of software performance as a  
142 function of axial position in the low density, high SNR dataset for best-in-class and representative  
143 middle-range software (**Fig. S4A**). We observed that a key cause of the spread in software

144 performance is variation in software performance away from the focal plane. Near the focal plane,  
145 most software packages perform well. However, the axial and lateral RMSE away from the plane of  
146 focus is significantly higher for the best in class software, and the Jaccard index is also slightly  
147 improved (**Fig. S4A**). This is also visibly apparent in the super-resolved images (**Fig. 4A**). We observed  
148 that best-in-class software had a Z-range (the FWHM range of axially resolved software recall,  
149 **Methods**) of 1170 nm, greater than two-thirds of the simulated range. Outside this range, the recall  
150 and Jaccard index dropped sharply, probably due the large increase in PSF size and decrease in  
151 effective SNR at large defocus (**Fig. S1**).

152 When we examined results for the low SNR, low density dataset (**Fig. 2A, 3F**), we found an expected  
153 two-fold degradation in best-in-class RMSE (lateral RMSE 39 nm, axial RMSE 60 nm), due to the  
154 decrease in image SNR. However, the best-in-class software (SMolPhot<sup>20</sup>) Jaccard index was  
155 effectively constant between the low and high SNR datasets (86 % vs 85 %), although the Z-range did  
156 drop at lower SNR (930 nm vs 1120 nm). The best astigmatism software packages were thus  
157 remarkably good at finding spots at low SNR, even away from the focal plane.

158 We compared best-in-class software performance to Cramér-Rao lower bound (CRLB) theoretical  
159 limits (**Fig. S5, S6, Supplementary Note 3**). Close to the focus, best-in-class software was near the  
160 CRLB (within 25 %), but significant deviations from the CRLB occurred > 200 nm (**Fig. S6**). This could  
161 be due to difficulty in distinguishing signal from false positives away from focus.

162 Astigmatic software performance dropped for the challenging high spot density datasets (**Fig. 2A, 3**).  
163 For the high SNR high spot density dataset (best software, SMolPhot), localization error increased  
164 and Jaccard index decreased significantly compared to the low density condition (lateral RMSE best  
165 HD 51 nm vs best LD 27 nm, axial RMSE best HD 66 nm vs best LD 29 nm, Jaccard index best HD 66 %  
166 vs best LD 85 %). Inspection of the super-resolved images (**Fig. S7**) nevertheless shows qualitatively  
167 acceptable results for the HD dataset, particularly in the lateral dimension. In some circumstances,  
168 the performance reduction at 10x higher spot density could be acceptable for 10x faster, potentially  
169 live-cell-compatible, imaging speed. We also observed a large spread of software performance for  
170 the high density datasets, probably because a significant fraction of the software packages were  
171 primarily designed for low density conditions.

172 We observed poor performance for the most challenging low SNR high spot density astigmatism  
173 dataset (**Fig. 2A, 3, S8**, best software SMolPhot). Best-in-class localization precision and Jaccard  
174 index decreased significantly (lateral RMSE 76 nm, axial RMSE 101 nm, Jaccard index 58 %). These  
175 data suggest that low SNR high density 3D astigmatic localization microscopy entails significant  
176 reduction in image resolution.

#### 177 *Double helix point spread function localization microscopy*

178 We next analyzed the performance of the double helix software (**Fig. 3D-F, S9A**). For the software in  
179 the high SNR low spot density condition, double helix software showed more uniform performance  
180 than astigmatism. Best-in-class software (SMAP-2018) showed only a limited improvement  
181 compared with average software (**Fig. 3D-F**, lateral RMSE, 27 nm best vs 37 nm average; axial RMSE  
182 21 nm best vs 34 nm average; Jaccard index 77 % best vs 73 % average). In general software  
183 localization performance was close to the CRLB (**Fig. S6**). We observed that performance of the  
184 software away from the focal plane is relatively uniform (**Fig. 4A, S4A**), and best-in-class Z-range at  
185 high SNR was large at 1180 nm (**Fig. S4A, Supplementary Table 2**). Double helix imaging may show  
186 less software-to-software variation and larger Z-range at low spot density than astigmatic imaging  
187 because the PSF shape and intensity are fairly constant as a function of Z; unlike astigmatic imaging,  
188 where spot size, shape and intensity vary greatly as a function of Z (**Fig. S1**).

189 Double helix software performance decreased significantly for the low spot density low SNR  
190 condition (best software, SMAP-2018), particularly in terms of best-in-class Jaccard index (66 % low

191 SNR vs 77 % high SNR, **Fig. 3D-E, S8, S9A**). DH Jaccard index was also significantly worse than  
192 astigmatism results at either high or low SNR (85 % high SNR, 86 % low SNR). This indicates that it  
193 was quite hard to successfully find localizations in the low SNR DH dataset, likely because the large  
194 size of the DH PSF spreads emitted photons over a large area, lowering effective image SNR. DH PSF  
195 designs with reduced Z-range but more compact PSF would likely be less sensitive to this issue<sup>21</sup>.

196 Double helix software performed poorly on the high spot density datasets at high SNR (best software  
197 CSpline<sup>22</sup>), especially in terms of the Jaccard index (**Fig. 3D-E, S9A**, best lateral RMSE 67 nm, best  
198 axial RMSE 69 nm, best Jaccard index 46 %). The poor performance at high spot density is again  
199 probably because the large DH PSF size increases spot density and decreases SNR (**Fig. S1**). DHPSF  
200 performance at high spot density and low SNR was also not reliable (**Fig. 3D-F, S9A**, best software,  
201 SMAP-2018).

## 202 *Biplane localization microscopy*

203 Best-in-class biplane software (SMAP-2018), at low spot density and for both high and low SNR,  
204 delivered the best performance in any modality (high SNR: lateral RMSE 12.3 nm, axial RMSE 21.7  
205 nm, Jaccard 87 %), despite a slightly decreased image SNR for the biplane simulations (**Methods**).  
206 We observed a large spread in software performance in terms of lateral RMSE and Jaccard index,  
207 with the best-in-class software significantly outperforming the other competitors (**Fig. S9B, 2D**). At  
208 low spot density, best-in-class biplane software (SMAP-2018) showed good performance as a  
209 function of Z, with high Jaccard index over almost the entire Z-range of the simulations, and with a Z-  
210 range of 1200 nm at high SNR (**Fig. S4AC, Supplementary Table 2**). The axial RMSE was relatively  
211 uniform as a function of Z and close to the CRLB limit (**Fig. S6**). As axial and lateral RMSE are both  
212 averaged over the entire Z-range, the strong biplane results arise from good performance across a  
213 large Z-range (**Fig. S4**).

214 At high spot density and high SNR, best-in-class biplane software (SMAP-2018) showed acceptable  
215 performance (**Fig. 3D-F, S7, S9B**, best lateral RMSE 43 nm, best axial RMSE 49 nm, best Jaccard index  
216 61 %). Uniquely among the 3D modalities, best-in-class biplane software also gave acceptable  
217 performance at high spot density and low SNR (**Fig. 3D-F, S7, S9B**, best lateral RMSE 55 nm, best  
218 axial RMSE 72 nm, best Jaccard index 61 %, best software SMAP-2018).

## 219 **Performance of 2D software**

220 We next assessed the performance of 2D SMLM software. For the pseudo-ER 2D dataset, at low  
221 density best-in-class software (ADCG<sup>23</sup>) performed substantially better than the class average  
222 (**Fig. S10, S11**, lateral RMSE 31 nm vs 36 nm average, Jaccard index 90 % best vs 72 %). Low density  
223 results for the brighter fluorophore microtubules dataset were similar to the dimmer pseudo-ER  
224 dataset (**Fig. S10, S12** best software SMolPhot). For the very high density 2D dataset, which had 25x  
225 higher spot density than the LD dataset, best-in-class software (ADCG) showed excellent  
226 performance (**Fig. S10**, lateral RMSE, 45.5 nm, Jaccard index 75%). Best-in-class performance (ADCG)  
227 on the dimmer fluorophore data at high spot density was also strong (**Fig. S10**, best lateral RMSE 51  
228 nm, best Jaccard index 70 %).

## 229 **Algorithms**

230 We identified several classes of algorithm participant software (**Supplementary Table 1**):

231 1) *Non-iterative* software regroups pixels in the local neighborhood of the candidates, like  
232 interpolation, center of mass (QuickPALM<sup>24</sup>) or template matching (WTM<sup>25</sup>). These often older  
233 algorithms are fast but tend to achieve poor performance.

234 2) *Single emitter fitting* software is usually built on a multi-step strategy of detection, spot  
235 localization, and optional spot rejection. The detection step finds bright spots in noisy images on the  
236 pixel grid. The selection of candidates is usually performed by local maximum search after a

237 denoising filter. Others rely on more complex algorithms like the wavelet transform (WaveTracer<sup>26</sup>).  
238 We did not observe software ranking to depend noticeably on the choice of optimization scheme:  
239 least-square, weighted least-square or maximum-likelihood estimator.

240 3) *Multi-emitter fitting* software groups clusters of overlapping spots, and simultaneously fits  
241 multiple model PSFs to the data. Typically, fitted spots are added to the cluster until a stopping  
242 condition is met<sup>4,5</sup>. This leads to improved localization performance at high spot density, at the cost  
243 of reduced speed. This class of software (e.g., 3D-DAOSTORM<sup>11</sup>, CSpline, PeakFit, ThunderSTORM<sup>27</sup>)  
244 was amongst the top performers in each 2D and 3D competition category.

245 As expected, single- and multiple-emitter fitting methods both performed well on low density data.  
246 For the 2D challenge, multi-emitter fitting showed a clear advantage over single emitter fitting at  
247 high density. Surprisingly however, well-tuned single-emitter fitting algorithms (SMolPhot, SMAP-  
248 2018) outperformed multi-emitter algorithms for the 3D high density conditions.

249 4) *Compressed sensing algorithms*. One subset of these algorithms utilize deconvolution with  
250 sparsity constraints to reconstruct super-resolved images<sup>28-30</sup>. Although deconvolution approaches  
251 can give good results, they are limited by the necessary use of a sub-pixel grid; increased localization  
252 precision requires smaller grid resolution, which must be balanced against increased computational  
253 time. Recent approaches address this issue by localizing the point sources in a gridless manner under  
254 some sparsity constraint (ADCG, SMfit, SOLAR\_STORM, TVSTORM<sup>31</sup>). This software class consistently  
255 gave the overall best performance for 2D high-density (ADCG 1<sup>st</sup>, FALCON<sup>30</sup> 2<sup>nd</sup>, SMfit 3<sup>rd</sup>).

256 5) *Other approaches*. Of the alternative algorithmic approaches used, the annihilating filter-based  
257 method LEAP<sup>32</sup> gave good performance for biplane imaging. Recently, we received the first challenge  
258 submission from a deep learning SMLM software (DECODE); these promising preliminary results are  
259 available on the competition website.

#### 260 *Post-hoc temporal grouping*

261 Because molecule on-time is stochastically distributed across multiple frames, a common post-  
262 processing approach to improve localization precision is to group molecules detected multiple times  
263 in adjacent frames, and average their position<sup>33</sup> (**Supplementary Note 4**). Temporal grouping was  
264 used by the top performers (including SMolPhot, MIATool<sup>34</sup> and SMAP-2018), and is visibly apparent  
265 as a more punctate super-resolved image (**Fig. 4A**).

#### 266 *Choice of PSF model*

267 Most software used a variant of Gaussian PSF model. A few participants designed more accurate PSF  
268 models. Either diffraction theory was used (MIATool, LEAP) or spline fitting of an analytical function  
269 to the experimental PSF was adopted (CSpline, SMAP-2018). Although simple Gaussian model PSFs  
270 were sufficient to obtain best-in-class performance for the 2D and astigmatic modalities (ADCG,  
271 PeakFit, SMolPhot), top results for the more optically complex biplane and double helix modalities  
272 were exclusively software using non-Gaussian PSF models (SMAP-2018, CSpline, MIATool, LEAP).

#### 273 *Multi-algorithm packages*

274 Several software packages take a Swiss army knife approach of integrating multiple optional  
275 localization algorithms into one program, to be flexible enough to suit various experimental  
276 conditions<sup>19,27</sup>. SMAP-2018 and ThunderSTORM achieved strong across-the-board performance  
277 supporting this rationale.

#### 278 *Software run time*

279 Software run time is important both for ease of use and real time analysis. We did not observe  
280 correlation between software localization performance (Efficiency) and software run time (**Fig.**

281 **S13A**). We thus created an alternative ranking metric, *Efficiency-Runtime*, which gave 25 % weighting  
282 to run time (**Supplementary Note 2.7, Fig S13B**). Many good performers in the efficiency-only  
283 ranking were relatively fast and thus retained good ranking (SMAP-2018, SMolPhot, 3D-  
284 DAOSTORM). Interestingly, two software packages highly optimized for speed gained top ranking in  
285 this analysis: pSMLM-3D<sup>35</sup> and QC-STORM.

#### 286 *Diagnostic tools for software and algorithm performance*

287 During our analysis, we frequently noticed common types of deviation between software results and  
288 ground truth which were easily diagnosed by visual inspection (**Fig. S14, S15**). This included not only  
289 obvious issues of poor localization precision or spot averaging at high density, but also more subtle  
290 problems such as a common error of structural warping which significantly reduced software  
291 performance. On the competition website, we provide detailed diagnostic software reports including  
292 multiple examples of software performance on individual frames to help developers to identify  
293 algorithm and software limitations and maximize software performance (**Fig. S3, S16**).

#### 294 **Assessment on real STORM data**

295 We investigated the performance of a representative subset of astigmatism software on real STORM  
296 datasets of well characterized test structures, microtubules and nuclear pore complex, NPC (**Fig. 4B,**  
297 **S17**). This qualitative assessment was consistent with findings for simulated data. No performance  
298 difference between single and multi-emitter fitters was observed, which is not surprising since spot  
299 density in these datasets was low. Relatively poor software performance was immediately obvious  
300 from visual inspection (QuickPALM). Temporal grouping noticeably improved resolution (3D-  
301 DAOSTORM, CSpline, MIATool, SMAP-2018). Gaussian fitting software . Interestingly, although  
302 Gaussian/ Bessel PSF modelling software (3D-DAOSTORM, MIATool, ThunderSTORM) gave high  
303 resolution images, software which modelled the experimental PSF via spline fitting (CSpline, SMAP-  
304 2018) gave noticeably improved resolution of fine structural features such as the top and bottom of  
305 the NPC (**Fig. 4B**) or the hollow core of antibody-labelled microtubules (**Fig. S17**).

#### 306 **DISCUSSION**

307 The strongest conclusion we draw from the 3D localization microscopy challenge is that choice of  
308 localization software greatly affects the quality of final super-resolution data, even at “easy” high  
309 SNR, low spot density conditions. Biplane performance was particularly dependent on software  
310 choice, with only one software (SMAP-2018) achieving near-Cramér-Rao lower bound performance.  
311 Double helix SMLM showed less sensitivity to choice of software than biplane, with astigmatic SMLM  
312 intermediate between the two. The best software in each modality performed close to the Cramér-  
313 Rao lower bounds over a wide focal range and successfully detected most molecules, even at low  
314 signal to noise. Average software in all three modalities was significantly worse, with the obtained  
315 axial resolution being particularly sensitive to software choice.

316 The second major conclusion is that localization software that explicitly includes the experimental  
317 PSF in the fitting model gives a significant performance increase for 3D SMLM. For the more optically  
318 complex biplane and double helix modalities in particular, the best results were from software which  
319 incorporated non-Gaussian PSF models (SMAP-2018, CSpline, MIATool). This result also highlights  
320 the importance of accurate PSF modelling in 3D SMLM simulations. The performance advantage of  
321 experimental PSF fitting software would not have been observable had simulations been generated  
322 with a simple Gaussian PSF.

323 Of the different algorithm classes, well-tuned single-emitter and multi-emitter fitting algorithms  
324 (each capable of dealing well with occasional molecule overlap) gave good results for low density 3D  
325 SMLM. We also found that several software packages for astigmatic or biplane imaging gave  
326 adequate performance for the challenging case of high molecule densities, as long as the image SNR  
327 was high. Current software packages gave poor performance when molecule density was high and

328 image SNR was low. These results indicate that with current algorithms high density 3D SMLM  
329 performance is mediocre at high SNR and poor at low SNR. Surprisingly, multi-emitter fitting did not  
330 show significant improvement over well-tuned single emitter fitting for the 3D high-density datasets;  
331 this may indicate that significant potential for improvement remains in this category.

332 Many software packages did not apply temporal grouping<sup>33</sup>, resulting in reduced software  
333 performance. Since temporal grouping is a simple step for maximum precision, we urge all software  
334 developers to integrate this approach into their software as an optional final step in the localization  
335 process.

336 The second 2D localization microscopy challenge provided the opportunity to reassess the state of  
337 the field. The performance of best-in-class 2D software over a range of conditions, at both high and  
338 low spot density, was very strong. Interestingly, the top three performers in the 2D high density  
339 condition were all compressed sensing algorithms (ADCG, FALCON, SMfit). In low density 2D  
340 conditions, the best single-emitter, multi-emitter and compressed sensing algorithms all gave  
341 comparable, excellent, performance. We speculate that performance in the low spot density 2D  
342 category might now be near optimal levels.

343 In future, we plan to extend the SMLM challenge into an open platform with a fully automated  
344 assessment process, and where new competition simulations and assessment metrics can easily be  
345 created and contributed by the community. It will be important to account for new technologies and  
346 developments in SMLM, such as scientific CMOS cameras<sup>6</sup>, in future simulations. It would also be  
347 exciting to adapt the tools developed in the SMLM challenge to other classes of super-resolution  
348 microscopy, such as fluorescence-fluctuation-based super-resolution microscopies (*e.g.*, 3B<sup>36</sup>, SOFI<sup>37</sup>,  
349 SRRF<sup>38</sup>) and structured illumination microscopy<sup>39</sup>.

350 The results of this competition show that the best 2D and 3D localization microscopy software have  
351 formidable algorithmic performance. However, a problem that often hinders adoption of new SMLM  
352 algorithms is that only a small subset of algorithms is packaged in, or compatible with fast, well-  
353 maintained, user-friendly software packages, which include all stages of the SMLM data analysis  
354 pipeline – analysis, visualization and quantification. This remains a key outstanding challenge for the  
355 field.

356 Both the 3D and 2D localization microscopy software challenges remain open and continuously  
357 updated on the competition website. This continuously evolving analysis of SMLM software  
358 performance provides software developers with a robust means of benchmarking new algorithms,  
359 and helps to ensure that super-resolution microscopists use software that gets the best out of their  
360 hard-won data.

361

## 362 ACKNOWLEDGEMENTS

363 *Authors acknowledge the following funding sources: a Newcastle University Research Fellowship and*  
364 *a Wellcome Trust & Royal Society Sir Henry Dale Fellowship grant number 206670/Z/17/Z to SH; an*  
365 *European Research Council (ERC) under the European Union's Horizon 2020 research and innovation*  
366 *programme, Grant Agreement no. 692726 to DS, TAP, MU; UK BBSRC grants BB/M022374/1,*  
367 *BB/P027431/1, BB/R000697/1 grant and MRC grants MC-UU-12018/2, MR/K015826/1 to RH;*  
368 *European Research Council (ERC) grant CoG-724489, CellStructure to JR; FranceBioImaging*  
369 *infrastructure ANR-10-INBS-04 to J.-B.S; National Institutes of Health grant 1R15GM128166-01 to*  
370 *GMH; and NSF SBIR grants 1353638, 1534745 to Double Helix LLC. We thank R. Piestun at University*  
371 *of Colorado for providing DH-PSF phase mask designs to Double Helix LLC. We thank all the*  
372 *localization microscopy challenge participants for their contribution: Hazen Babcock (3D-DAOSTORM,*  
373 *Cspline, L1H), Fabian Hauser (3D-STORM Tools), Shigeo Watanabe (3D-WTM,WTM), Nicholas Boyd*  
374 *(ADCG), Junhong Min, Kyong Jin and Jong Chul Ye (ALOHA, FALCON), Hervé Rouault (B-recs),*  
375 *Emmanuel Soubies (CELO-STORM), Artur Speiser, Srinivas Turagas and Jakob Macke (DECODE), Alex*  
376 *von Diezmann, Camille Bayas and W. E. Moerner (Easy-DHPSF), Thomas Vomhof and Jochen Reichel*  
377 *(FIRESTORM), Hanjie Pan (LEAP), Ann Wheeler (Localizer), Zhen-li Huang and Yujie Wang*  
378 *(MaLiang), J. Chao, R. Velmurugan, A. V. Abraham and R. J. Ober (MIATool), Hendrik Deschout*  
379 *(mlePALM), Thomas Pengo (Octane, PeakSelector), Yi-na Wang (PALMER), Alex Herbert*  
380 *(PeakFit), Koen Martens and Johannes Hohlbein (pSMLM-3D), Luchang Li (QC-STORM), Ricardo*  
381 *Henriques (QuickPALM), G. Tamas and J. Sinko (RainSTORM), Steve Wolter and Markus Sauer*  
382 *(RapidSTORM), Manfred Kirchgessner and Frederik Gruell (SFP Estimator), Yiming Li and Jonas Ries*  
383 *(SMAP), Hayato Ikoma (SMfit), A. Loot, A. Valdmann, M. Eltermann, M. Kree and M. Pärs*  
384 *(SMolPhot), Yoon J. Jung, Anthony Barsic Rafael Pietsun, and Nikta Fakhri (SOLAR\_STORM), Anna*  
385 *Archetti (STORMChaser), Martin Ovesny, Guy Hagen and Pavel Krizek (ThunderSTORM), Jiaqing*  
386 *Huang (TVSTORM), Adel Kechkar, Corey Butler and Jean-Baptiste Sibarita (WaveTracer) and Benoît*  
387 *Lelandais (ZOLA-3D). We thank the SMLMS 2016 organizers (S. Manley and A. Radenovic, EPFL) for*  
388 *hosting a localization microscopy challenge special session. We also thank Double Helix LLC and*  
389 *Molecular Devices LLC for sponsoring the SMLMS 2016 special session. The sponsors had no input or*  
390 *influence on the research.*

## 391 AUTHOR CONTRIBUTIONS

392 DS and SH conceived and coordinated the study. DS, SH, TAP, AAr, HB, SC, AW, GMH, RH, TL, TP, JBS  
393 designed the study. SH, AAg, RH, JBS collected experimental PSFs. DS, TAP, SH, TL wrote simulation  
394 code. BR shared unpublished software. DS generated simulated datasets. JR shared experimental  
395 STORM data. AH, JR, JC, RV provided feedback and quality control on simulations and analysis  
396 methods. TAP carried out the assessment of software performance. TAP, DS, SH analysed  
397 and interpreted the results. DS, HB, RO, BR, GMH, JBS, JR, RH, MU, SH directed research. SH, DS, TAP  
398 wrote the manuscript with feedback from all authors.

## 399 REFERENCES

- 400 1. Betzig, E. *et al.* Imaging Intracellular Fluorescent Proteins at Nanometer Resolution. *Science*  
401 **313**, 1642–1645 (2006).
- 402 2. Hess, S. T., Girirajan, T. P. K. & Mason, M. D. Ultra-High Resolution Imaging by Fluorescence  
403 Photoactivation Localization Microscopy. *Biophys. J.* **91**, 4258–4272 (2006).
- 404 3. Rust, M. J., Bates, M. & Zhuang, X. Sub-diffraction-limit imaging by stochastic optical  
405 reconstruction microscopy (STORM). *Nat Methods* **3**, 793–795 (2006).
- 406 4. Holden, S. J., Uphoff, S. & Kapanidis, A. N. DAOSTORM: an algorithm for high- density super-  
407 resolution microscopy. *Nat Meth* **8**, 279–280 (2011).
- 408 5. Huang, F., Schwartz, S. L., Byars, J. M. & Lidke, K. A. Simultaneous multiple-emitter fitting for  
409 single molecule super-resolution imaging. *Biomed. Opt. Express* **2**, 1377–1393 (2011).

- 410 6. Huang, F. *et al.* Video-rate nanoscopy using sCMOS camera-specific single-molecule  
411 localization algorithms. *Nat. Methods* **10**, 653–658 (2013).
- 412 7. Sage, D. *et al.* Quantitative evaluation of software packages for single-molecule localization  
413 microscopy. *Nat. Methods* **12**, 717–724 (2015).
- 414 8. Huang, B., Jones, S. A., Brandenburg, B. & Zhuang, X. Whole-cell 3D STORM reveals  
415 interactions between cellular structures with nanometer-scale resolution. *Nat Meth* **5**, 1047–1052  
416 (2008).
- 417 9. Shtengel, G. *et al.* Interferometric fluorescent super-resolution microscopy resolves 3D  
418 cellular ultrastructure. *Proc. Natl. Acad. Sci.* **106**, 3125–3130 (2009).
- 419 10. Huang, B., Wang, W., Bates, M. & Zhuang, X. Three-Dimensional Super-Resolution Imaging  
420 by Stochastic Optical Reconstruction Microscopy. *Science* **319**, 810–813 (2008).
- 421 11. Babcock, H., Sigal, Y. M. & Zhuang, X. A high-density 3D localization algorithm for stochastic  
422 optical reconstruction microscopy. *Opt. Nanoscopy* **1**, 1–10 (2012).
- 423 12. Ovesný, M., Křížek, P., Švindrych, Z. & Hagen, G. M. High density 3D localization microscopy  
424 using sparse support recovery. *Opt. Express* **22**, 31263–31276 (2014).
- 425 13. Min, J. *et al.* 3D high-density localization microscopy using hybrid astigmatic/ biplane  
426 imaging and sparse image reconstruction. *Biomed. Opt. Express* **5**, 3935–3948 (2014).
- 427 14. Zhang, S., Chen, D. & Niu, H. 3D localization of high particle density images using sparse  
428 recovery. *Appl. Opt.* **54**, 7859–7864 (2015).
- 429 15. Juette, M. F. *et al.* Three-dimensional sub-100 nm resolution fluorescence microscopy of  
430 thick samples. *Nat. Methods* **5**, 527–529 (2008).
- 431 16. Pavani, S. R. P. *et al.* Three-dimensional, single-molecule fluorescence imaging beyond the  
432 diffraction limit by using a double-helix point spread function. *Proc. Natl. Acad. Sci.* **106**, 2995–2999  
433 (2009).
- 434 17. Collaboration through competition. *Nat. Methods* **11**, 695 (2014).
- 435 18. Annibale, P., Vanni, S., Scarselli, M., Rothlisberger, U. & Radenovic, A. Quantitative Photo  
436 Activated Localization Microscopy: Unraveling the Effects of Photoblinking. *PLOS ONE* **6**, e22678  
437 (2011).
- 438 19. Li, Y. *et al.* Real-time 3D single-molecule localization using experimental point spread  
439 functions. *Nat. Methods* (2018). doi:10.1038/nmeth.4661
- 440 20. Loot A. , Valdmann A., Eltermann M., Kree M., Pärs M. SMolPhot Software. Available at:  
441 <https://bitbucket.org/ardiloot/>. (Accessed: 28th January 2019)
- 442 21. Grover, G., DeLuca, K., Quirin, S., DeLuca, J. & Piestun, R. Super-resolution photon-efficient  
443 imaging by nanometric double-helix point spread function localization of emitters (SPINDLE). *Opt.*  
444 *Express* **20**, 26681–26695 (2012).
- 445 22. Babcock, H. P. & Zhuang, X. Analyzing Single Molecule Localization Microscopy Data Using  
446 Cubic Splines. *Sci. Rep.* **7**, 552 (2017).
- 447 23. Boyd, N., Schiebinger, G. & Recht, B. The Alternating Descent Conditional Gradient Method  
448 for Sparse Inverse Problems. *SIAM J. Optim.* **27**, 616–639 (2017).
- 449 24. Henriques, R. *et al.* QuickPALM: 3D real-time photoactivation nanoscopy image processing in  
450 ImageJ. *Nat Meth* **7**, 339–340 (2010).
- 451 25. Takeshima, T., Takahashi, T., Yamashita, J., Okada, Y. & Watanabe, S. A multi-emitter fitting  
452 algorithm for potential live cell super-resolution imaging over a wide range of molecular densities. *J.*  
453 *Microsc.* **271**, 266–281 (2018).
- 454 26. Kechkar, A., Nair, D., Heilemann, M., Choquet, D. & Sibarita, J.-B. Real-Time Analysis and  
455 Visualization for Single-Molecule Based Super-Resolution Microscopy. *PLOS ONE* **8**, e62918 (2013).
- 456 27. Ovesný, M., Křížek, P., Borkovec, J., Švindrych, Z. & Hagen, G. M. ThunderSTORM: a  
457 comprehensive ImageJ plug-in for PALM and STORM data analysis and super-resolution imaging.  
458 *Bioinformatics* **30**, 2389–2390 (2014).
- 459 28. Soubies, E., Blanc-Féraud, L. & Aubert, G. A Continuous Exact l0 Penalty (CELO) for Least  
460 Squares Regularized Problem. *SIAM J. Imaging Sci.* **8**, 1607–1639 (2015).

- 461 29. Babcock, H. P., Moffitt, J. R., Cao, Y. & Zhuang, X. Fast compressed sensing analysis for super-  
462 resolution imaging using L1-homotopy. *Opt. Express* **21**, 28583–28596 (2013).
- 463 30. Min, J. *et al.* FALCON: fast and unbiased reconstruction of high-density super-resolution  
464 microscopy data. *Sci. Rep.* **4**, 4577 (2014).
- 465 31. Huang, J., Sun, M., Ma, J. & Chi, Y. Super-Resolution Image Reconstruction for High-Density  
466 Three-Dimensional Single-Molecule Microscopy. *IEEE Trans. Comput. Imaging* **3**, 763–773 (2017).
- 467 32. Pan, H., Simeoni, M., Hurley, P., Blu, T. & Vetterli, M. LEAP: Looking beyond pixels with  
468 continuous-space Estimation of Point sources. *Astron. Astrophys.* **608**, A136 (2017).
- 469 33. Durisic, N., Laparra-Cuervo, L., Sandoval-Álvarez, Á., Borbely, J. S. & Lakadamyali, M. Single-  
470 molecule evaluation of fluorescent protein photoactivation efficiency using an in vivo nanotemplate.  
471 *Nat. Methods* **11**, 156–162 (2014).
- 472 34. Chao, J., Ward, E. S. & Ober, R. J. A software framework for the analysis of complex  
473 microscopy image data. *IEEE Trans. Inf. Technol. Biomed. Publ. IEEE Eng. Med. Biol. Soc.* **14**, 1075–  
474 1087 (2010).
- 475 35. Martens, K. J. A., Bader, A. N., Baas, S., Rieger, B. & Hohlbein, J. Phasor based single-  
476 molecule localization microscopy in 3D (pSMLM-3D): An algorithm for MHz localization rates using  
477 standard CPUs. *J. Chem. Phys.* **148**, 123311 (2017).
- 478 36. Cox, S. *et al.* Bayesian localization microscopy reveals nanoscale podosome dynamics. *Nat.*  
479 *Methods* **9**, 195–200 (2012).
- 480 37. Dertinger, T., Colyer, R., Iyer, G., Weiss, S. & Enderlein, J. Fast, background-free, 3D super-  
481 resolution optical fluctuation imaging (SOFI). *Proc. Natl. Acad. Sci.* **106**, 22287–22292 (2009).
- 482 38. Gustafsson, N. *et al.* Fast live-cell conventional fluorophore nanoscopy with ImageJ through  
483 super-resolution radial fluctuations. *Nat. Commun.* **7**, (2016).
- 484 39. Gustafsson, M. G. L. Surpassing the lateral resolution limit by a factor of two using structured  
485 illumination microscopy. SHORT COMMUNICATION. *J. Microsc.* **198**, 82–87 (2000).
- 486

## 487 METHODS

### 488 1. CHALLENGE ORGANIZATION

489 We first ran the 3D SMLM software challenge as a time limited competition, with a results session  
490 hosted as a special session of the 6<sup>th</sup> Annual Single Molecule Localization Microscopy Symposium in  
491 August 2016. The competition has now been converted to a permanent software challenge  
492 accepting new submissions. Special thanks is due to the software SMAP and 3D-WTM<sup>25</sup> that  
493 participated in all eight categories (*density x modality*). The current list of participants is at:

494 <http://bigwww.epfl.ch/smlm/challenge2016/index.html?p=participants>

495 All datasets, methods, participations, and results of the challenge 2016 made available at  
496 <http://bigwww.epfl.ch/smlm/challenge2016/>. Software for simulation and analysis is hosted on the  
497 competition GitHub repository: <https://github.com/SMLM-Challenge/Challenge2016/>

498 A Life Sciences Reporting Summary is associated with this manuscript on the Nature Methods  
499 website.

### 500 2. LOCALIZATION MICROSCOPY SIMULATIONS

#### 501 2.1. Structure, noise levels and spot densities

502 *Structure.* The synthetic datasets were designed to be similar to images derived from real cellular  
503 structures . We defined mathematical models for cellular structures that imitate cytoskeletal  
504 filaments such as microtubules and larger tubular structures such as the endoplasmic reticulum or  
505 mitochondria (**Fig. S18A**). These structures have a tubular shape in the 3D space. For the 3D  
506 competition, we simulated synthetic 25 nm diameter microtubules (**Fig. 1**). Pseudo-microtubules are  
507 defined with their central axis elongating in a 3D space having an average outer diameter of 25 nm  
508 with an inner, hollow tube of 15 nm diameter. For the 2D competition, in addition to synthetic  
509 microtubules (MT), we simulated larger diameter 150 nm cylinders, called pseudo-endoplasmic  
510 reticulum (pseudo-ER), designed to approximate larger cellular structures such as mitochondria and  
511 the endoplasmic reticulum (ER) (**Fig. 1**).

512 The underlying sample structure is formalized in a continuous space which allows rendering of digital  
513 images at any scale, from very high resolution (up to 1 nm/pixel) to low resolution (camera  
514 resolution: 100 nm/ pixel). The continuous-domain 3D curve is represented by means of a  
515 polynomial spline. The sample is imaged in a  $6.4 \times 6.4 \mu\text{m}^2$  field of view, and the center lines of the  
516 microtubules have limited variation along the z (vertical) axis, *i.e.*, less than  $1.5 \mu\text{m}$ . The fluorescent  
517 markers are uniform randomly distributed over the structure according to the required density. The  
518 photon emission rate of each fluorophore is controlled by a photo-activation model (see below). The  
519 exact locations of all fluorophores are stored at high precision floating-point numbers expressed in  
520 nanometers. This ground-truth file is used for conducting objective evaluations without human bias.

521 *Noise levels.* We generated data at three different signal-to-noise ratio (SNR) levels, based on real  
522 signal to noise levels encountered under common SMLM experimental scenarios: *N1*, fixed cells  
523 antibody labelled with organic dye<sup>10</sup>, high signal, medium background; *N2*, fluorescent protein  
524 labelling<sup>1</sup>, low signal, low background; and *N3*, live cell affinity dye labelling<sup>40,41</sup>, high signal, high  
525 background.

526 *Spot density.* As performance at different density of active emitters is a key challenge for SMLM  
527 software, we generated 3D competition datasets at both sparse emitter density  
528 ( $0.25 \text{ mol. [molecule] } \mu\text{m}^{-2}$ ), *3D LD* and high emitter density ( $2.5 \text{ mol. } \mu\text{m}^{-2}$ ), *3D HD*. For the 2D  
529 competition, we generated a sparse ( $0.5 \text{ mol. } \mu\text{m}^{-2}$ ), *2D LD*, and very high density dataset  
530 ( $5 \text{ mol. } \mu\text{m}^{-2}$ ), *2D HD*.

531 Together, these simulated conditions closely resemble experimental 3D and 2D data under a range  
532 of challenging conditions of SNR, spot density, axial thickness and structure summarized in  
533 **Supplementary Table 3**. In addition, we provide simulated z-stacks of bright beads for software  
534 calibration. The competition datasets (**Supplementary Table 4**) are available online on the  
535 competition website.

536

## 537 **2.2. Photophysics activation model**

538 We incorporated a 4-state model of fluorophore photophysics<sup>18</sup>, including a transient dark state (dye  
539 blinking) and a bleaching pathway (**Fig. S18C**). Given a list of source locations from the structure  
540 simulator, fluorophore blinking was simulated by a 4-states Markov chain model. The states are ON,  
541 OFF, BLEACH, DARK and the transitions are Poisson distributed (**Fig. S18C**), except for the OFF to ON  
542 transitions which follow a uniform random distribution to reflect that in typical experimental  
543 conditions, constant imaging density is maintained by tuning the photoactivation rate during the  
544 experiment. All switching is calculated at sub-frame resolution and then total fluorophore on-time  
545 was integrated over each frame.

546 Due to two decay paths, the actual mean lifetime of the state ON is

$$T_{LIFETIME} = \frac{1}{\frac{1}{T_{ON}} + \frac{1}{T_{BLEACH}}}$$

547 Switching rates were chosen to approximate photoactivatable fluorescent proteins  $T_{ON}=3$  frames,  
548  $T_{DARK}=2.5$  frames, and  $T_{BLEACH}=1.5$  frames.

549 Fractional fluorophore ON-times per frame (between 0 and 1) were multiplied by the mean flux of  
550 photon emission. The flux of photons expressed in photons/seconds was given by the relation

$$F = \frac{\Phi P \sigma}{e}$$

551  $\Phi$  is the quantum yield of the dye,  $P$  is power of the laser in W/cm<sup>2</sup>,  $e = h c / \lambda$  is the energy of one  
552 photon,  $\sigma = 1000 \ln(10) \epsilon / N_A$  is the absorption cross section in cm<sup>2</sup> and  $\epsilon$  is the molar extinction  
553 coefficient (EC) or absorptivity in cm<sup>2</sup>/mol which is a characteristic of a given fluorophore. The laser  
554 power was Gaussian distributed over the field of view. At the end of this process a list of XY  
555 positions, on-frames and (noise-free) intensities for all activated fluorophores was obtained.

556 Analysis of the resulting simulated photon counting distribution is presented in **Supplementary**  
557 **Note 5** and **Figure S23**.

## 558 **2.3. Experimental Point Spread Function**

559 Model PSFs, stored as high resolution look up tables, were derived from experimentally measured  
560 PSFs. Although the algorithmic approach is distinct, the concept of accurately modelling the  
561 experimental PSF based on calibration data bears relation to the PSF phase retrieval approach  
562 previously employed by Hanser and coworkers<sup>42</sup>.

563 Images of fluorescent beads were recorded for each modality (**Supplementary Table 5**). Signal to  
564 noise ratio of recorded PSFs was maximized in all cases by maximizing exposure time and averaging  
565 over several frames to increase dynamic range.

566 To acquire experimental PSFs, we took 100 nm Tetraspek beads (Invitrogen) adsorbed to #1.5  
567 (170  $\mu$ m thick) coverglass, imaged in water. The excitation wavelength was between 640 nm and 647  
568 nm, and a Cy5 emission filter was used. Data acquisition parameters for each modality are listed in  
569 **Supplementary Table 5**.

570 The experimental PSFs used to generate the simulated data are available on the competition  
571 website. As the goal of this study was to compare software obtained on typical SMLM microscopes,  
572 we deliberately chose PSFs representative of common implementations of each 3D modality.  
573 However, additional PSF engineering should improve results of any specific modality, for example  
574 adaptive-optics corrected astigmatism<sup>43</sup>, or reduced Z-range, higher SNR DH-PSF designs<sup>21</sup>.

575 The experimental point spread functions used here were measured for fluorescent beads adsorbed  
576 to the microscope cover slip, and should be appropriate simulations of SMLM data acquired within a  
577 few microns of the cover slip. Performing SMLM imaging at greater depths, *e.g.*, in tissue or even  
578 deep within single cells, with oil immersion objectives will cause spherical aberration due to  
579 refractive index mismatch<sup>44</sup>. In order to accurately simulate SMLM data acquired at depth, the  
580 experimental PSFs could be acquired at a matching depth, by embedding fluorescent beads in  
581 agarose. Alternatively, the PSF for beads at the coverslip could be measured and explicitly calculated  
582 via phase retrieval, and then convolved with the appropriate degree of spherical aberration<sup>44</sup>.

583

## 584 **2.4. Simulation PSF construction**

585 For each modality, 3-6 beads were selected within a small (< 32  $\mu\text{m}$ ) region, to minimize PSF  
586 variation due to spherical aberration. Images for each selected bead were interpolated in XY to a  
587 pixel size of 10 nm. Beads were then coaligned by cross-correlation on the in-focus frame. Coaligned  
588 beads were averaged in XY to minimize pixel quantization artefacts and to increase SNR. Where  
589 necessary, Z-stacks were interpolated to a Z-step size of 10 nm. A central Z-range of 1.5  $\mu\text{m}$  was  
590 selected that represents 151 optical planes with a Z-step of 10 nm. The Z-range covers -750 nm to  
591 +750 nm. The plane of best focus was chosen as the simulation 0 nm plane. Each model PSF was  
592 normalized such that the total intensity of the PSF in the in-focus frame within a diameter of 3  
593 FWHM from the PSF center was equal to 1.

594 For the DH PSF, the transmission of the combined phase mask system was measured as 96 %, which  
595 was approximated as 100 % brightness relative to the 2D and astigmatic PSFs.

596 In biplane super-resolution microscopy, emitted fluorescence is split into two simultaneously imaged  
597 channels, with a small (500-1000 nm) defocus introduced between the two channels<sup>15</sup>. As the small  
598 defocus should introduce minimal additional aberration into an optical system, we semi-  
599 synthetically constructed a realistic biplane PSF from the experimental 2D PSF. The two defocused  
600 PSFs were constructed by duplicating the 2D PSF and offsetting it by -250 nm and 250 nm for each Z-  
601 plane.

602 This yielded five high SNR model PSFs with an isotropic voxel size of 10x10x10 nm<sup>3</sup>.

603 The ground truth XY=0 was defined as the image center of mass of the in-focus frame of the model  
604 PSF, and Z=0 was defined as the in-focus frame. Accounts for shifts in the fitted XY center of the  
605 model PSF by localization software due to systematic offsets and Z-dependent variation of the model  
606 PSF center of mass are dealt with below (wobble correction).

## 607 **2.5. Noise model**

608 A constant mean autofluorescent background was added to the noise-free simulated images, and  
609 these images were then fed through the noise model representing Poisson distributed fluorescence  
610 emission recorded on a high quantum efficiency back-illuminated EMCCD<sup>45,46</sup>.

611 The proposed noise model assumed as main contributions to the stochastic noise:

- 612
- 613 •  $\sigma_S$ , the shot noise produced by the fluorescence background and signal and the spurious charge. Shot noise can be derived from the second moment of the Poisson distribution

- 614 •  $\sigma_R$ , the read noise of EMCCD camera, which is described by second moment of the Gaussian  
615 distribution  
616 •  $\sigma_{EM}$ , the electron multiplication noise introduced by the gain process, which is described by  
617 the second moment of the Gamma distribution<sup>46</sup>.  
618

619 We assumed as camera parameters the ones specified for the Photometrics Evolve Delta 512 EMCCD  
620 camera (values for other manufacturer's EMCCDs are similar):

- 621 • QE = 0.9, Evolve quantum efficiency at 700 nm absorption wavelength.  
622 •  $\sigma_R = 74.4$  electrons, manufacturer measured root mean square noise for Evolve 512 camera  
623 •  $c = 0.002$  electrons, manufacturer quoted spurious charge (clock induced charge only, dark  
624 counts negligible)  
625 •  $EM_{gain} = 300$   
626 •  $e_{adu} = 45$  electron per analog to digital unit (ADU), analog to digital conversion factor  
627 •  $G = 0.9 \cdot 300 / 45 = 6$ , total system gain  
628 • BL = 100 ADU

629 The final simulated photon electrons will thus be given by:

$$n_{ie} = \mathcal{P}(QE \cdot n_{photIn} + c)$$

$$n_{oe} = \Gamma(n_{ie}, EM_{gain}) + \mathcal{G}(0, \sigma_R)$$

630 which leads to the final pixel counts:

$$ADU_{out} = \min\left(\frac{n_{oe} - n_{oe} \bmod e_{ADU}}{e_{peradu}} + BL, 65535\right)$$

## 631 2.6. Depth-dependent lateral distortion/ wobble

632 As the PSF models are experimentally derived, the 3D estimated localizations exhibit a depth-  
633 dependent lateral distortion, here called *wobble*. This optical distortion is due to a combination of a  
634 systematic offset (arbitrary definition of PSF center) and optical aberrations<sup>47</sup>. In order to compare  
635 estimated and true localizations, we correct this effect during the assessment (**Methods 3.1**).

## 636 2.7 Comparison of software results between different modalities.

637 The intensities of the PSF in each imaging modality were normalized to facilitate comparison of  
638 results between different modalities. Software results between 2D, 3D AS and 3D DH modalities are  
639 expected to be directly comparable.

640 For the biplane model PSF, as the emitted fluorescence is split into two channels, the intensity in  
641 each of the two simulated biplane channels was additionally reduced by 50 %. We note that a  
642 simulation bug meant that the fluorescence background was not reduced by 50 % as intended,  
643 leading to artificially high background for the biplane simulation. *I.e.*, the background in each of the  
644 two biplane channels is the same as in the single channel of the other modalities. However, due to  
645 the low background level in the 3D simulations, the effect on image SNR and thus localization error  
646 is small (see **Fig. S5, S6**), less than 5 nm near the plane of focus. Therefore, as long as the small drop  
647 in image SNR is taken into account, approximate comparisons of the biplane data to the other  
648 modalities can still be made.

## 649 3. SOFTWARE ASSESSMENT

### 650 3.1 Protocol

651 Each localization file submitted by the participants was manually checked for erroneous systematic  
652 errors in the definition of the dataset coordinate system, such as offsets, XY axis flips or clear scaling

653 errors. Datasets were then programmatically standardized into a consistent output format. All  
654 modifications are publicly available. If required, the modifications consisted of columns reordering,  
655 reversing axes, XY axis swap, and shifting the lateral positions by a half camera pixel.

656 The assessment pipeline includes three main parts: localization processing, the pairing between true  
657 and estimated localization and the metrics calculations. The first one depends on the assessment  
658 settings. There are two switchable properties: photon thresholding and wobble correction. Their  
659 combinations yield four different assessment settings. Up to 64 assessment runs per software were  
660 possible (*i.e.*, 4 modalities, 4 datasets per modality). For any setting, we excluded the fluorophores  
661 within a lateral distance of 450 nm from the border. This value corresponds to the radius of the  
662 largest PSF, *i.e.*, Double Helix. The activations too close from the border are more difficult to localize  
663 and could bias the results.

664 The pairing between true and estimated localizations was performed frame by frame. For every  
665 frame, we identified the localizations that are close enough to a ground-truth position as true-  
666 positives (TP), the spurious localizations as false-positives (FP) and the undetected molecules as  
667 false-negatives (FN). The procedure matches two sets of localizations. We deployed the presorted  
668 nearest-neighbor search for its efficiency, with a linking threshold of 250 nm. The results are  
669 effectively similar to the computationally intensive Hungarian algorithm<sup>7</sup>.

#### 670 *Photon thresholding*

671 A photon threshold was required primarily due to the use of a realistic fluorophore blinking model.  
672 Since a fluorophore could activate/ bleach at any point in a simulated frame, this led to many frames  
673 containing very dim, undetectable localizations, *e.g.*, where a molecule had been active for one or  
674 more frames previously, and then bleached during the first 5 % of a frame. These fractional  
675 localizations should also be present but practically undetectable in an experimental dataset.

676 We decided to focus the software analysis on the localizations where the molecule was active for the  
677 majority of a frame, to be consistent with experimental expectations. Therefore, we implemented a  
678 photon threshold means where we kept the 75% brightest ground truth fluorophore activations.  
679 Because this was performed *after* the pairing step, observed localizations that were paired to  
680 discarded ground truth activations were also removed from the metric calculations.

#### 681 *Wobble correction*

682 The centroid of experimental point spread functions shifts laterally by as much as 50 nm, as a  
683 function of axial position<sup>10,47</sup>. This is most often ignored by localization software, and instead  
684 corrected post-hoc by reference to a calibration curve<sup>37</sup>. Since our simulated PSF is experimentally  
685 derived, it was necessary to correct for these artefactual shifts between the observed localizations  
686 and ground truth, as part of the assessment process. This correction was performed using calibration  
687 data uploaded by competitors, similar to the correction typically performed on experimental data<sup>47</sup>.

688 Three scenarios were proposed to the participants: no correction was applied during the  
689 assessment; the correction was based on a file provided by the participant itself or the correction  
690 was calculated by ourselves. The latter nevertheless requires the participant to localize a stack of  
691 beads we provided. Since the true positions of the beads are known, the difference between the  
692 estimated and true positions could be calculated and averaged. It thus yields the values for wobble  
693 correction.

694 In certain specific cases (identified on the competition website), at the request of authors, we did  
695 not apply this correction, for example because the software explicitly considered the whole 3D PSF  
696 during fitting and was thus immune to this lateral shift artefact. For accurate results, application of  
697 lateral shift correction is critical for analysis of localization microscopy simulations using

698 experimentally derived PSFs, as can be seen by comparison of typical software results with and  
699 without wobble correction (**Fig. S19**).

### 700 **3.2 Metrics**

701 We calculated a large number of analysis metrics to quantify the performance of software relative to  
702 ground truth. These are discussed in detail in **Supplementary Note 2**. The metrics are split into two  
703 categories: localization based and image based metrics.

704 *Localization based metrics.* This directly relies on the localizations positions and notably includes the  
705 Recall, the Precision, the Jaccard Index, the RMSE (axial and lateral) and the consolidated Z-range.  
706 For the calculation of average software performance (**Fig. 3D-F, S10**) outlier software with an  
707 efficiency less than  $eff=0$  ( $eff=-30$  for 3D high density dataset) were excluded from the  
708 measurement. The key metrics of assessment were:

709 1. *Root mean squared localization error (RMSE).* The foremost consideration for localization  
710 software is how accurately it finds the position of labelled molecules. This was quantified as  
711 the root mean squared difference between the measured molecule position,  $x_i^s$ , and the  
712 ground truth position,  $x_i^t$ , in both the lateral (XY) and axial (Z) dimensions.

713 
$$RMSE \text{ lateral (RMSE Lateral) [nm]: } \sqrt{\frac{1}{TP} \sum_{i \in SN_T} (x_i^s - x_i^t)^2 + (y_i^s - y_i^t)^2}.$$

714 
$$RMSE \text{ axial (RMSE Axial) [nm]: } \sqrt{\frac{1}{TP} \sum_{i \in SN_T} (z_i^s - z_i^t)^2}.$$

715 2. *Jaccard index (JAC, %).* In addition to localization precision, SMLM image resolution depends  
716 critically on number of localized molecules<sup>48</sup>, so it is crucial for SMLM software to accurately  
717 detect a large fraction of molecules in a dataset, and minimize false localizations. For every  
718 frame, we identified the localizations that are close enough to a ground-truth position as  
719 true-positives (TP), the spurious localizations as false-positives (FP) and the undetected  
720 molecules as false-negatives (FN). We then computed the *Jaccard index* (JAC, %), which  
721 measures the fraction of correctly detected molecules in a dataset,

$$JAC = 100 \frac{TP}{TP + FP + FN}$$

722 3. *Efficiency (E).* For ranking purposes, we developed a single summary statistic for overall  
723 evaluation of software performance, which we term the *efficiency (E)*, encapsulating both  
724 the software's ability to find molecules, measured by the Jaccard index, and the software's  
725 ability to precisely localize molecules.

$$E = 100 - \sqrt{(100 - JAC)^2 + \alpha^2 RMSE^2}$$

726 The trade-off between these two metrics is controlled by a parameter  $\alpha$ . In a retrospective  
727 analysis, we chose  $\alpha = 1 \text{ nm}^{-1}$  for the lateral efficiency  $E_{lat}$ ,  $\alpha = 0.5 \text{ nm}^{-1}$  for the axial efficiency  
728  $E_{ax}$ , based on the linear regression slope between the localization errors and Jaccard index  
729 (**Fig. S20J-K**). Using this definition, an average software performance has an efficiency in the  
730 range 25-75, a perfect software would have the maximum efficiency of 100. Overall 3D  
731 efficiency was calculated as the average of lateral and axial efficiencies. Overall software  
732 rankings (**Fig. 2**) were calculated as the sum of rankings for high and low SNR datasets.

733 *Image based metrics.* The image based metrics are computed from a rendered image and includes  
734 the Signal-to-Noise Ratio (SNR) and the Fourier Ring / Shell Correlation (FRC/FSC). To render the  
735 image, we added the contribution of each localized molecule at the corresponding pixels. A  
736 contribution takes the form of a 3D additive Gaussian with a Full-Width Half Maximum (FWHM) of  
737 20 nm. A complete list of all computed metrics is presented in the **Supplementary Note 2**.

738 We also calculated localization based metric results as a function of axial position. We proceeded by  
739 considering a subset of activations lying within an interval of axial positions (*i.e.*, from the true

740 localizations). Then, most of the metrics (*e.g.*, Recall) are locally computed. This yields a curve  
741 providing information on the depth performance of each software / modality.

742 In order to summarize software axial performance, we analyzed how the recall varied as a function  
743 of Z. A typical recall versus axial position curve (**Fig. S4**) will drop at positions far from the focal  
744 plane, *i.e.*, where software can no longer detect spots to defocus. We first smoothed the curve using  
745 a sliding window. Then we computed the software Z-range, defined as the full width half maximal  
746 Recall of the smoothed curve (**Fig. S21**). This quantity is visually intuitive and useful for discussion of  
747 the recall performance if considered alongside a plot of recall vs axial position. However, because  
748 FWHM recall depends on the maximal recall, ranking based on this procedure would promote a  
749 software which poorly performed everywhere (*i.e.*, flat curve), whereas a software which performed  
750 well in the focal plane but less well outside would obtain a worse FWHM recall. This observation  
751 leads us to produce a so-called consolidated Z-range, by multiplying the Z-range value by the  
752 maximal Recall, which should provide a robust metric that avoids the previous case scenario.

753 *Principal component analysis.* In order to analyse the relationship between analysis metrics we  
754 computed the covariance matrix between each metric (**Fig. S22A**) and the principal component  
755 analysis (PCA) on the metrics (**Fig. S22B-D**). Each metric was standardized before applying the  
756 covariance and the PCA. For convenience, we took the additive inverse of the metrics for which  
757 lower values are best (*i.e.*, FP, FN, RMSE, FRC, FSC).

758 Summary statistics and detailed results for each software are available on the competition website  
759 (<http://bigwww.epfl.ch/smlm/challenge2016/index.html?p=results>), which also includes a tool for  
760 side-by-side comparison of the results of multiple software packages

### 761 **3.3 Baseline Localization Software**

762 We developed a minimalist Java tool software that performs localizations of bright emitters on the 4  
763 modalities of the challenge 2016: 2D, Astigmatism, Double-Helix, and Biplane. This  
764 SMLM\_BaselineLocalization software is only designed to establish the performance baseline for the  
765 SMLM challenge. It has intentionally limited lines of code and relies only on few threshold  
766 parameters to localize particles. It has basic calibration tool that has to run on a z-stack of beads to  
767 find the linear  $f(x)$  relation between the axial position Z and the shape of the bead.

- 768 • Astigmatism:  $Z = f(W_x - W_y)$ , where  $W_x$  and  $W_y$  are respectively an estimation of the size in X  
769 and Y.
- 770 • Double-Helix:  $Z = f(\theta)$ , where  $\theta$  is the angle formed the pairing of two close points.
- 771 • Biplane:  $Z = f(W_{\text{left}} - W_{\text{right}})$ , where  $W_{\text{left}}$  and  $W_{\text{right}}$  are respectively an estimation of the size of  
772 the spots in left and the right plane.

773 The Java code is available: <https://github.com/SMLM-Challenge/Challenge2016>

## 774 **4 REAL DATA ASSESSMENT**

775 Astigmatism software was tested on previously published real 3D STORM datasets of microtubules  
776 and nuclear pore complex<sup>19</sup>. The tubulin dataset corresponds to the raw data for **Fig. S6** in Ref <sup>19</sup>,  
777 and the nuclear pore complex dataset corresponds to raw data for **Fig. S9** in Ref <sup>19</sup>. Key acquisition  
778 parameters for data analysis are summarized on the competition website.

779 Data were analyzed by software authors or expert users, and submitted via the competition website.  
780 All data were drift corrected via cross-correlation. STORM images were rendered with a constant  
781 Gaussian blur with 3 nm standard deviation and saturated by 0.1 – 0.5 %. The complete scripts used  
782 for assessment and image rendering are available on the competition GitHub page.

783 **5 DATA AVAILABILITY**

784 **5.1 Data availability statement**

785 Simulated competition datasets are available at <http://bigwww.epfl.ch/smlm/challenge2016/>,  
786 together with the parameters used to generate the data. The ground truth list of simulated molecule  
787 positions for each competition dataset remains secret in order to allow the software challenge to  
788 remain continuously open to new submissions. However, ground truth data are available for the  
789 simulated training datasets.

790 Raw data for this study are uploaded on the Nature Methods website. The data corresponding to  
791 specific figures are listed with the Supplementary information.

792 **5.2 Code availability statement**

793 All software is available at <https://github.com/SMLM-Challenge/Challenge2016>

794 **REFERENCES, ONLINE METHODS**

- 795 40. Carlini, L. & Manley, S. Live Intracellular Super-Resolution Imaging Using Site-Specific Stains.  
796 *ACS Chem. Biol.* **8**, 2643–2648 (2013).
- 797 41. Shim, S.-H. *et al.* Super-resolution fluorescence imaging of organelles in live cells with  
798 photoswitchable membrane probes. *Proc. Natl. Acad. Sci.* **109**, 13978–13983 (2012).
- 799 42. Hanser B. M., Gustafsson M. G. L., Agard D. A. & Sedat J. W. Phase-retrieved pupil functions  
800 in wide-field fluorescence microscopy. *J. Microsc.* **216**, 32–48 (2004).
- 801 43. Izeddin, I. *et al.* PSF shaping using adaptive optics for three-dimensional single-molecule  
802 super-resolution imaging and tracking. *Opt. Express* **20**, 4957–4967 (2012).
- 803 44. McGorty, R., Schnitzbauer, J., Zhang, W. & Huang, B. Correction of depth-dependent  
804 aberrations in 3D single-molecule localization and super-resolution microscopy. *Opt. Lett.* **39**, 275–  
805 278 (2014).
- 806 45. Hirsch, M., Wareham, R. J., Martin-Fernandez, M. L., Hobson, M. P. & Rolfe, D. J. A Stochastic  
807 Model for Electron Multiplication Charge-Coupled Devices – From Theory to Practice. *PLOS ONE* **8**,  
808 e53671 (2013).
- 809 46. Basden, A. G., Haniff, C. A. & Mackay, C. D. Photon counting strategies with low-light-level  
810 CCDs. *Mon. Not. R. Astron. Soc.* **345**, 985–991 (2003).
- 811 47. Carlini, L., Holden, S. J., Douglass, K. M. & Manley, S. Correction of a Depth-Dependent  
812 Lateral Distortion in 3D Super-Resolution Imaging. *PLoS ONE* **10**, e0142949 (2015).
- 813 48. Baddeley, D. & Bewersdorf, J. Biological Insight from Super-Resolution Microscopy: What We  
814 Can Learn from Localization-Based Images. *Annu. Rev. Biochem.* **87**, 965–989 (2018).
- 815

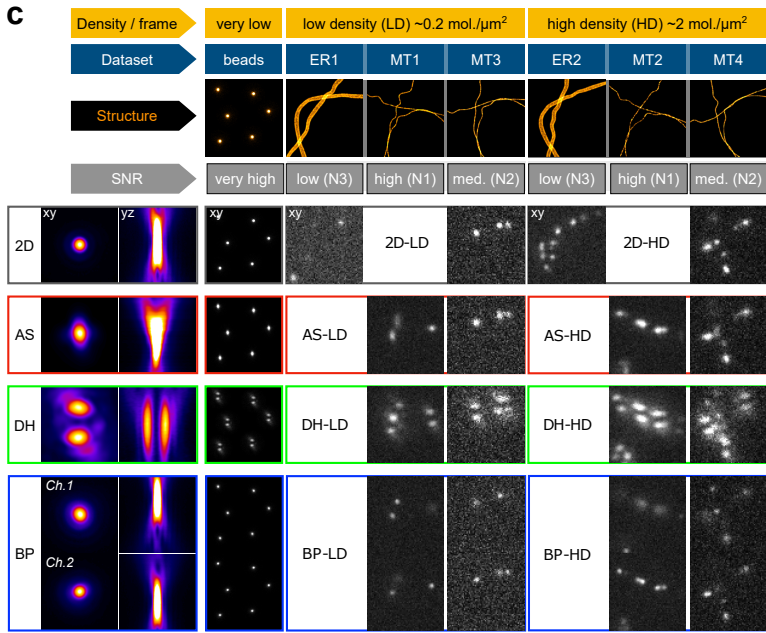
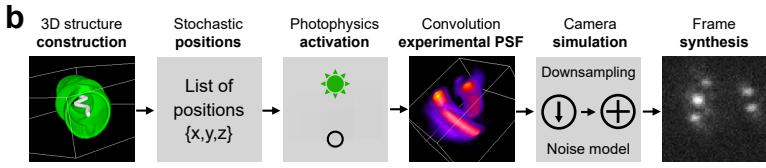
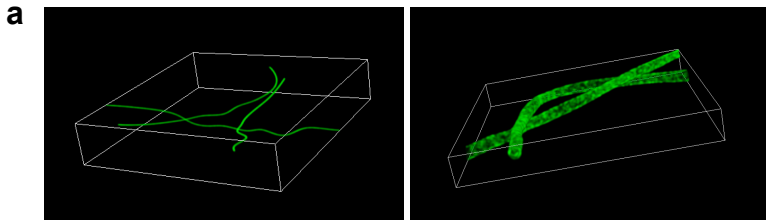
816 **FIGURE LEGENDS**

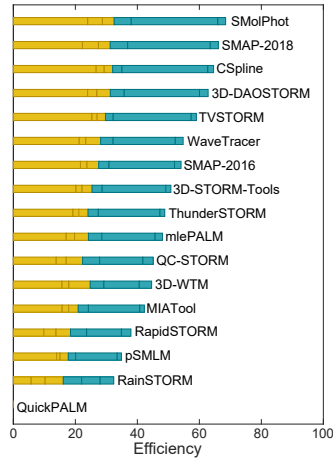
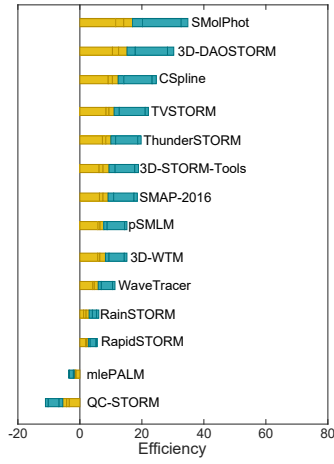
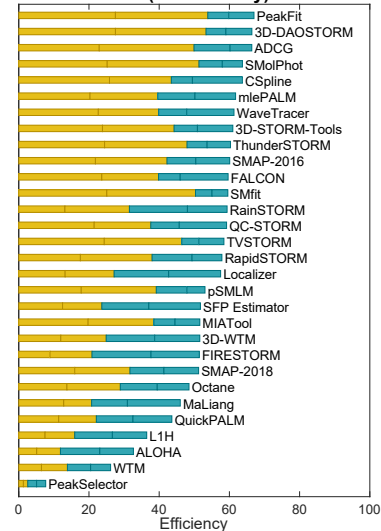
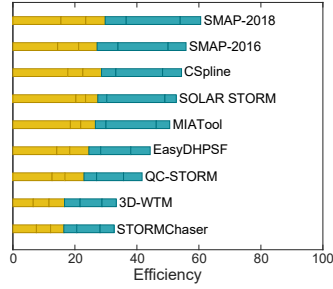
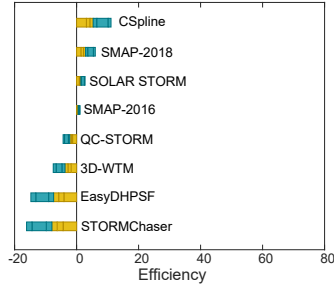
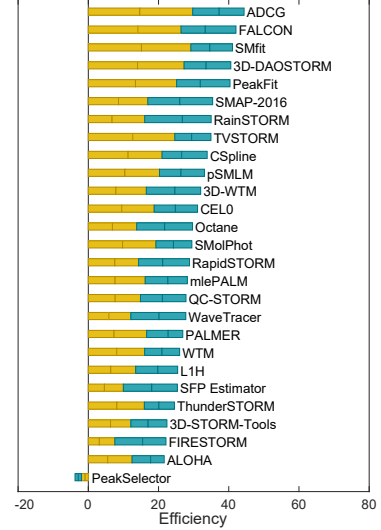
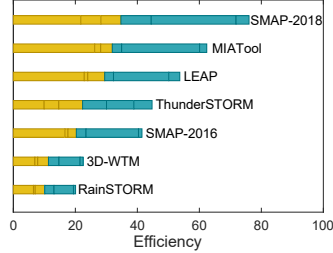
817 **Figure 1: Summary of SMLM challenge simulations.** **A.** 3D rendering of simulated microtubules and  
818 endoplasmic reticulum samples. **B. Key simulation steps.** The structure is constructed from 3D tubes  
819 continuously defined by three B-spline functions in the volume of interest. Membranes of the tubes  
820 are densely populated with possible positions. Fluorophores follow a 4-state photophysics model.  
821 Activations of a given frame are convolved with the experimental PSF and shot & camera noise is  
822 added. **C.** Summary of all 16 challenge datasets, calibration data and experimental PSFs. Left column:  
823 orthogonal projections of the experimentally-derived PSF. Right column: exemplar frame for each  
824 competition dataset, characterized by structure (endoplasmic reticulum, E; microtubules, MT),  
825 modality (2D; astigmatism, AS; double helix, DH; biplane, BP), density (low density, LD; high density,  
826 HD) and SNR (noise level N1, N2, N3). *BP Ch. 1,2*, indicates two biplane channels with a relative focal  
827 shift of 500 nm.

828 **Figure 2: Leaderboards for each competition modality, at low and high spot density.** Ranking is based  
829 on software Efficiency, which combines Jaccard index (fraction of successfully detected molecules)  
830 and localization precision (RMSE, root mean square error, lateral & axial). Orange, contribution of  
831 high SNR dataset; blue, contribution of low SNR dataset.

832 **Figure 3: Comparison of 3D software performance.** Gold stars indicate top performers for each  
833 dataset. Dashed lines in top, middle panels indicate overall efficiency (higher is better). **A-C.**  
834 Localization error and spot detection performance of all astigmatic SMLM software. **D-E.** Average  
835 (colored marker with *s.d.* error bars, sample sizes for each category indicated in **Supplementary**  
836 **Table 2**) and best-in-class (colored marker with gold star) software performance for all competition  
837 modalities. *AS, astigmatism; DH, double helix; BP, biplane.*

838 **Figure 4: Super-resolved images of software results for simulated and real competition datasets.** **A.**  
839 *Xy and xz projection images of 3D competition datasets for representative software. Top: best-in-*  
840 *class software in each modality, for high SNR low density dataset. Bottom: representative average*  
841 *software. Left: xy and xz overview images for winning AS software. Middle: xy and xz zoom images of*  
842 *boxed regions in left panel, for winning and mid-range software, each modality. Right: xy and xz line*  
843 *profiles of winning and mid-range software for each modality, for boxed regions in middle panel.*  
844 *Image colors: red, ground truth; green, software results. Line profiles: GT, ground truth, black; AS,*  
845 *astigmatism, red; BP, biplane, blue; DH, double helix, green. Panel key: Software-name Dataset-*  
846 *ranking°. Scale bar: full image, 1  $\mu$ m, magnified regions, 100 nm. **B. Astigmatism software results for***  
847 *real nuclear pore complex 3D STORM data. Top: Super-resolved overview image in xy for 3D-*  
848 *DAOSTORM software, color coded for depth. Bottom: xz orthoslices along 600 nm wide dashed*  
849 *region indicated in top panel for 8 astigmatism software packages. Scale bars, 500 nm.*



**a Astigmatism (Low Density)****Astigmatism (High Density)****d 2D (Low Density)****b Double-Helix (Low Density)****Double-Helix (High Density)****2D (High Density)****c Biplane (Low Density)****Biplane (High Density)**